Mn promotion of rutile TiO2-RuO2 anodes for water oxidation in acidic media

Applied Catalysis B: Environmental 261 (2020) 118225

Contents lists available at ScienceDirect

Applied Catalysis B: Environmental

journal homepage: www.elsevier.com/locate/apcatb

Mn promotion of rutile TiO_2-RuO_2 anodes for water oxidation in acidic media

Marco Etzi Coller Pascuzzi, Andrey Goryachev, Jan P. Hofmann*, Emiel J.M. Hensen*

Laboratory for Inorganic Materials and Catalysis, Department of Chemical Engineering and Chemistry, Eindhoven University of Technology, P.O. Box 513, 5600 MB, Eindhoven, The Netherlands

ARTICLE INFO

Keywords:
Water splitting
Oxygen evolution reaction
RuO_2
TiO_2
Manganese

ABSTRACT

A method to reduce noble metal content in oxygen-evolving electrocatalysts suitable to work in acidic media is presented. TiO_2-RuO_2 anodes can be promoted by Mn, resulting in increased activity and stability. The most active composition displayed an overpotential of 386 mV at a current density of 10 mA cm^{-2}, and a Tafel slope of 50 mV dec^{-1}. This anode only included 17 at% Ru out of the total amount of metals included in the film. We investigated the influence of Mn addition to TiO_2-RuO_2 on the structure, morphology, and surface area, and related differences to catalytic activity and stability. We found that increased porosity of the anode film by Mn addition and Mn inclusion in the TiO_2-RuO_2 lattice can explain the enhanced catalytic activity. A detailed characterization of fresh and used anodes provided insight into structural modifications induced by electrochemical treatment.

1. Introduction

Concerns about CO_2 emissions associated with burning fossil fuels to cover the ever-increasing global energy demand require breakthroughs in renewable energy solutions [1]. Clean energy from wind turbines and solar photovoltaics will increasingly contribute to the global energy supply. As these sources are highly variable and cannot be predicted well, there is a growing need to store electricity for successive use. Among the available energy carriers, hydrogen has attracted a lot of interest because of its high gravimetric energy density and the possibility to use it as a fuel in electrochemical cells with important applications for transportation and stationary power generation.

As the direct conversion of sunlight into hydrogen is still limited by the relatively low efficiency and stability of photoelectrochemical devices or photocatalysts [2–4], a promising alternative is to use electrolysis of water to convert (clean) electricity into chemical energy [5]. In a water electrolyzer, water is split into hydrogen and oxygen. Of the two half-reactions, the oxygen evolution reaction (OER), which takes place at the anode, is considered a bottleneck because of its slow kinetics due to the involvement of four protons and four electrons in the reaction mechanism [6,7]. Anodic overpotentials are usually around three times higher than the overpotentials at the cathode, where the relatively simple and fast hydrogen evolution reaction (HER) takes place [8]. The development of active and stable catalysts for anodic OER is crucial in order to improve the efficiency of the whole water splitting process. In the case of alkaline electrolysis, first-row transition metals, and particularly their oxides and oxyhydroxides, are promising OER electrocatalysts [9–11]. The use of Ni [12–16], Co [17–21], and Mn [22–26] has been investigated in depth, and the preparation and development of such electrocatalysts has been optimized so well that in some cases their performance is even better than that of IrO_2 and RuO_2 in alkaline environment [8,27–29].

However, in acidic media, relevant primarily to Proton Exchange Membrane (PEM) electrolyzers [30,31], the activity and stability of 3d metal oxides/oxyhydroxides are insufficient for large-scale applications. In these cases, only the rutile oxides IrO_2 and RuO_2 display sufficient stability, in particular when they are mixed with (rutile) TiO_2, acting as a stabilizer. These so-called Dimensionally Stable Anodes (DSA®) are employed for the large-scale electrochemical production of chlorine (chlor-alkali process) and oxygen [32–34]. However, in a hydrogen economy, it would be desirable to have anodes with the same performance but at a lower cost. Many strategies have been applied to reduce the noble metal content in the composition of DSAs®. The fabrication of IrO_2 and RuO_2 nanoparticles has been investigated as it allows for exposure of a larger number of active sites to the electrolyte while keeping the amount of active phase constant [35–39]. Another promising option is to add first-row transition metals in the composition of the electrodes. Ni [40,41], Co [42], Fe [43], and Zn [44] have been used in most of the cases as dopants for RuO_2. Typically, only small amounts of these elements are added to iso-structurally replace Ru

* Corresponding authors.
E-mail addresses: j.p.hofmann@tue.nl (J.P. Hofmann), e.j.m.hensen@tue.nl (E.J.M. Hensen).

https://doi.org/10.1016/j.apcatb.2019.118225
Received 25 June 2019; Received in revised form 19 September 2019; Accepted 22 September 2019
Available online 23 September 2019

atoms in the rutile lattice of RuO_2. In the case of manganese, instead, mixed ruthenium and manganese oxides have been shown to be active and stable electrocatalysts for the oxygen evolution reaction in alkaline media [45,46]. Only in a few studies, the effect of Mn addition on the performance of DSA®-type electrodes in the acidic OER has been reported [47–49], but a comprehensive structural and electrochemical characterization is needed to understand the reasons behind the activity and stability changes. In the present work, we addressed this issue by studying the influence of manganese on mixed Ti-Ru oxide electrodes in acidic water oxidation, establishing composition and activity trends. We emphasize the impact of manganese on the structure and the catalytic performance of TiO_2-RuO_2 anodes.

2. Experimental

2.1. Preparation of mixed TiO_2-RuO_2 electrodes

The preparation of TiO_2-RuO_2 anodes was carried out according to a procedure reported elsewhere [50]. Briefly, titanium tetraisopropoxide (Sigma-Aldrich, 97%) and ruthenium(III) chloride hydrate (Sigma-Aldrich, ruthenium content 38% minimum) were used as precursors. Ti to Ru atomic ratio was kept close to the composition of industrial DSA® anodes (70:30). 2,4-pentanedione (Alfa Aesar, 99%), a chelating agent, was added to the solution (2.5 $mmol/mmol_{Ti+Ru}$) in order to prevent a fast hydrolysis of the precursors. The concentration of the precursor salts was then adjusted to 1M by dilution with a 2:1 by volume ethanol/water mixture. The resulting solution was then stirred overnight prior to deposition.

Titanium foil (Advent, purity 99.6+ %, thickness 0.25 mm) was used as a substrate. Before deposition, the Ti foils were washed in acetone and sonicated for 15 min and, finally, rinsed with ethanol and deionized water. The solution was deposited on the cleaned Ti substrates by using a spin coater (SPS-Europe). Spin coating was performed at 4000 rpm for 15 s. The deposition area was limited to 1 cm^2. As-prepared anodes were dried in air at 80 °C for 10 min and calcined at 500 °C in static air for 2 h.

2.2. Mn incorporation

In order to investigate the effect of Mn addition on the electrocatalytic performance of the DSA® anodes, manganese chloride tetrahydrate (Sigma-Aldrich, ACS reagent ≥ 98%) was added to the previously described 1 M solution of the Ti-Ru precursor. The concentration of Mn^{2+} was chosen to be either 0.1, 0.5, 0.8, or 1.5 mol/L. Further preparation of Mn-containing anodes was done in the same manner as described above. The composition of the precursor solutions, the atomic composition of the as-prepared anodes, and sample names are summarized in Table 1.

2.3. Characterization of MnO_x-TiO_2-RuO_2 electrodes

X-ray diffraction (XRD) patterns were obtained using a Bruker D2 Phaser diffractometer equipped with a Cu K_α radiation source. The diffractograms were recorded with a step size of 0.02° and an acquisition time of 1 s, in the 2θ range of 10° to 70°.

Field-emission scanning electron micrographs (FESEM) were taken using an FEI Quanta 3D FEG microscope at an accelerating voltage of 5 kV without additional coating of the surface.

Energy dispersive X-Ray (EDX) spectrometry was performed in a Phenom Pro-X microscope with an accelerating voltage of 15 kV.

X-ray photoelectron spectroscopy (XPS) measurements were carried out on a K-Alpha XPS spectrometer (Thermo Scientific) equipped with a monochromatic Al K_α (1486.6 eV) X-ray source. The spot size was 400 µm and the pass energy was set at 200 eV and 50 eV for survey and region scans, respectively. Spectra were calibrated by setting the binding energy of the RuO_2 (Ru $3d_{5/2}$) component equal to 280.6 eV [51]. Fitting of the XPS spectra was performed using CasaXPS software.

XPS depth profiles were recorded on the same spectrometer by Ar^+ ion sputtering (3 kV, high-current). The duration of the sputtering steps was 4 min and XPS spectra were taken after each sputtering cycle. The depth profiles of each element were normalized to the highest intensity. In-plane and out-of-plane homogeneity of the samples was checked by XPS mapping and XPS depth profiling, respectively (*see ESI*). Ru 3d, Mn 2p, and Ti 3p regions were used to determine the content of RuO_2, MnO_x, and Ti^0, respectively. Due to the high reducibility of RuO_2 under ion sputtering conditions, no deconvolution of the Ru 3d region was performed and the area of the entire region was used to construct a profile. Profiles of MnO_x were constructed in the same way. The Ti 3p region was used instead of the Ti 2p region due to the overlap of the latter with Ru 3p peaks. The Ti^0 peaks (binding energy, BE ≈32.9 eV) were used to track the location of the titanium substrate.

Table 1
Sample names, concentrations of the precursors in the starting solutions and nominal atomic ratio of the metals.

Sample	Intended loading			Nominal metal composition		
	$Ti(i\text{-}OPr)_4$, mol/L	$RuCl_3$, mol/L	$MnCl_2$, mol/L	Ti, at%	Ru, at%	Mn, at%
Mn00	0.7	0.3	0.0	70	30	0
Mn09	0.7	0.3	0.1	64	27	9
Mn33	0.7	0.3	0.5	47	20	33
Mn44	0.7	0.3	0.8	39	17	44
Mn60	0.7	0.3	1.5	28	12	60

2.4. Electrochemical characterization

Electrochemical measurements were carried out in a standard three-electrode cell at room temperature with an Autolab PGSTAT302N potentiostat (Metrohm Autolab B.V.). Ti-supported films with a geometric area of 1 cm^2 were used as working electrodes (WE). Anodic currents of the bare Ti foil were found to be negligible in the range of the applied potentials (Fig. S1a, b), making it unnecessary to mask the back of the working electrodes. A platinum foil (area: 5 cm^2) was used as a counter electrode and an Ag/AgCl electrode (Radiometer Analytical, E_{RE} = +0.24 V) was used as a reference electrode, if not mentioned otherwise. 0.1 M H_2SO_4 (H_2SO_4 Sigma Aldrich, 99.999%) was used as electrolyte in all the tests. Milli-Q water (18.2 MΩ cm) was used in all the cleaning and dilution steps. All potentials are *iR*-corrected and reported *versus* the Reversible Hydrogen Electrode (RHE). Current densities are normalized using the geometric areas, if not mentioned otherwise.

The catalytic activity was evaluated by linear sweep voltammetry (LSV) recorded with a scan rate of 0.5 mV s^{-1} in the anodic direction. The values of overpotential at current densities of 1 and 10 mA cm^{-2} were used to compare the activity of the catalysts. Overpotentials (η) were calculated using the following equation:

$$\eta_{OER} = V_{meas} + V_{Ag/AgCl} + 0.059\,pH - E^{o}_{OER} \quad (1)$$

where V_{meas} is the measured potential, $V_{Ag/AgCl}$ is the potential of the reference electrode, and E^{o}_{OER} = +1.23 V is the standard electrode potential for the Oxygen Evolution Reaction. The as-recorded voltammograms were used to construct Tafel plots, where we evaluated the Tafel slopes (with an error ± 1 mV dec^{-1}).

Chronopotentiometry (CP) at a constant current density of 1 mA cm^{-2} and duration of 6 h was employed to assess the stability of the catalysts. The solutions were stirred during the measurements to avoid the accumulation of bubbles on the electrode surface.

Electrochemical impedance spectroscopy (EIS) was carried out in a frequency range of 10^{-1} to 10^5 Hz with an amplitude of 10 mV at the open circuit potential. The system was simulated with an $R_s(R_{ct}C_{dl})$

circuit using Nova 1.10 software, where R_s represents the electrolyte resistance, R_{ct} the charge transfer resistance, and C_{dl} the double layer capacitance of the electrode The values of the Electrochemical Surface Area (ECSA) were calculated from the ratio of the double layer capacitances with the specific capacitance. For the latter, we employed a constant value of 35 μF cm^{-2} for all prepared electrodes, in accordance with literature [8,27].

When current densities were normalized using the values of ECSA, this is specifically mentioned reporting the values in "mA cm^{-2}_{ECSA}" in the manuscript.

Long-term electrochemical stability of the samples Mn00 and Mn44 was evaluated by chronoamperometry at $E = +1.80$ V_{RHE} for 17 h. The amounts of dissolved Ru, Ti and Mn were determined by ICP-OES measurement of the spent electrolytes.

2.5. Characterization of spent electrolytes

The amount of Ru, Mn and Ti ions in the spent electrolytes was determined by ICP analysis. Inductively coupled plasma optical emission spectrometry (ICP-OES) was performed on a SPECTROBLUE EOP spectrometer equipped with an axial plasma source (Ar). The following emission lines were used: 240.3 nm and 267.9 nm (Ru), 257.6 nm and 259.4 nm (Mn), 334.9 nm and 336.1 nm (Ti).

2.6. Online electrochemical mass spectrometry (OLEMS) measurements

OLEMS measurements were carried out in a three-electrode EC glass cell equipped with a Red Rod reference electrode (Radiometer Analytical, $E_{RE} = +0.225$ V) and a Pt plate counter electrode. The working electrode slides with an average size of 0.5 cm^2 were mounted into a PEEK holder and contacted from the top by a gold wire enclosed in a quartz tube. Ar-purged 0.1 M H_2SO_4 (H_2SO_4 Sigma Aldrich, 99.999 %) was used as electrolyte. The temperature of the cell was maintained at 25 °C by a thermostat. EC treatment was performed using an Ivium Compactstat potentiostat (Ivium Technologies). OLEMS measurements were conducted on a quadrupole mass spectrometer (Balzers Quadstar, Prisma QME 200) at an operating pressure of approximately $4 \cdot 10^{-7}$ mbar. The OLEMS tip was equipped with a porous PTFE plug with a probing area of 0.79 mm^2. The tip was approached to the surface of the working electrode at a distance of ca. 20 μm by a micrometer screw with the help of a video microscope. The working electrode (WE)-tip distance was optimized for the highest intensity of the O_2^+ ion current ($m/z = 32$) measured during the OER. A more detailed description of the utilized OLEMS setup is given elsewhere [52,53].

Faraday plots [52,53] (*i.e.* gas production *vs.* faradaic charge) were constructed by plotting integrated ion currents of relevant ions (proportional to the amount of evolved gases) *versus* anodic charge supplied in the form of potential pulses (step size: 10 mV). Ion currents of $m/z = 32$ (O_2^+) and $m/z = 34$ ($H_2O_2^+$) were continuously recorded throughout the experiments. Potential pulses were separated by resting periods (open circuit, $j = 0$ mA cm^{-2}), necessary to achieve temporal separation of individual OLEMS peaks.

3. Results and discussion

3.1. Structural characterization of fresh electrodes

The influence of Mn addition on the phase composition of the electrodes was evaluated by XRD (Fig. 1). The reflections of the Ti substrate remain visible in all XRD patterns. Sample Mn00 contains a single rutile phase, demonstrating that a solid solution of TiO_2 and RuO_2 was formed [50,54]. Upon addition of Mn, a gradual shift of the rutile peaks towards higher diffraction angles is seen, which can be explained by a contraction of the unit cell. This change is due to the incorporation of Mn (IV) in the solid TiO_2-RuO_2 solution [49]. The ionic radii of Mn (IV), Ti(IV) and Ru(IV) are 67 pm, 74.5 pm, and 76 pm,

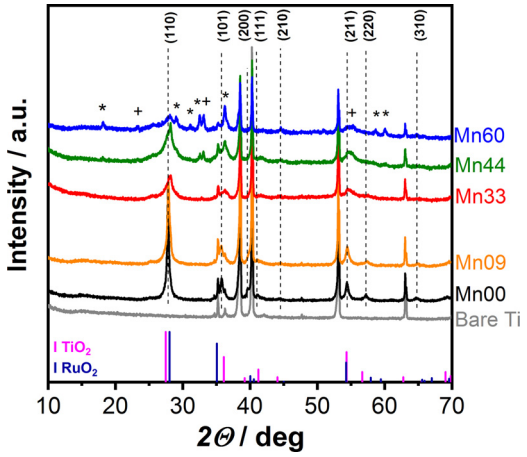

Fig. 1. X-ray diffractograms of the mixed TiO_2-RuO_2 samples. Dashed lines indicate the rutile peaks of the solid solution formed by TiO_2 (JCPDS#21-1276) and RuO_2 (JCPDS#40-1290). [*] Mn_3O_4 (JCPDS#24-0734), [+] Mn_2O_3 (JCPDS#41-1442) peaks.

respectively. As the differences in ionic radii among the elements are less than 15%, we can expect that Mn can easily enter into the solid solution of TiO_2-RuO_2. For Mn09 and Mn33 with a low Mn content, no diffraction patterns characteristic of Mn-oxides could be observed. This does not exclude the presence of very small domains of Mn-oxides or amorphous Mn-oxides. Samples with a higher Mn content (Mn44 and Mn60) exhibit diffraction peaks of Mn_3O_4 and Mn_2O_3. Thus, part of the Mn has segregated into separate Mn-oxide phases. The XRD patterns also show that a Mn content of the film higher than 9 at% results in a decrease of the rutile peak intensities, suggesting that the film becomes increasingly disordered due to the presence of Mn, as previously reported for RuO_2 – MnO_x electrodes [45].

The oxidation state of manganese was investigated by XPS. As Mn 2p region of mixed MnO_x compounds is composed of broad overlapping features with nearly similar BE (binding energy) values due to the multiplet splitting of Mn 2p (*e.g.* Mn(II) – 641.4 eV, Mn(III) – 641.4 eV, Mn(IV) – 641.8 eV) [55], we focused on Mn 3s spectra to determine the chemical composition and oxidation state of Mn in the samples (Fig. S2a). The Mn 3s peak is split due to exchange coupling between the 3s hole and the 3d electrons of Mn [56]. For the interpretation of these spectra, we followed the relevant literature [24,56–59]. The observed splitting values for samples Mn33, Mn44, and Mn60 range from 5.22 to 5.40 eV (Table S1), typical for Mn (II) and Mn (III) [56–58]. This is in keeping with the presence of Mn_3O_4 and Mn_2O_3 derived by XRD patterns of these samples.

The lower splitting for sample Mn09 (5.05 eV) indicates an overall increase in the oxidation state of Mn, which can be attributed to the additional presence of Mn in higher oxidation state (Mn (IV), splitting value 4.5 eV). This result is consistent with the insertion of part of the Mn in the TiO_2 – RuO_2 solid solution as Mn (IV), as discussed above.

For two selected samples, Mn00 and Mn44, survey spectra and fitted Ru 3d spectra are reported (Fig. 2a, b). The analysis of the Ru 3d spectra of Mn00 and Mn44 samples, done in accordance with the model proposed by Morgan [51], shows that Ru is present in form of RuO_2 (BE $Ru3d_{5/2} = 280.6 \pm 0.2$ eV). Apart from the two RuO_2 main peaks (Ru $3d_{5/2}$ and Ru 3d Ru $3d_{3/2}$), we can also see two characteristic features (BE $Ru3d_{5/2\ sat.} \approx 282.5$ eV) which can be ascribed to RuO_2 satellite peaks. The asymmetry of the RuO_2 lines is due to its metallic conductive nature. The absence of Cl-related peaks in Ru 3d ($RuCl_3 \cdot xH_2O$, BE Ru $3d_{5/2} = 282.2$ eV) and survey spectra (BE Cl 2p ≈ 200 eV) indicates that the Ru and Mn precursors were completely converted into oxides. Survey spectra show that the samples contain Ti, Ru, O, C and Mn (the latter only for Mn44), with no other elements present in detectable amounts. The presence of adventitious carbon (visible in the Ru 3d

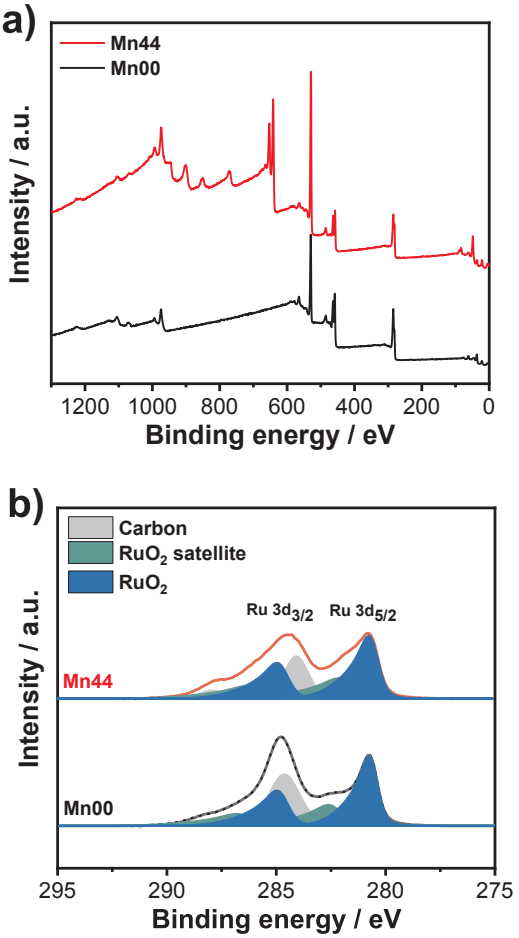

Fig. 2. a) Survey and b) Ru 3d XPS spectra of samples Mn00 and Mn44. Grey components in the Ru 3d region are related to C 1s peaks.

spectra) can be explained by the fact that the samples were handled in air [60]. The metal content at the surface of samples Mn00 and Mn44 are reported in Table S2. Mn00 shows the same Ti:Ru ratio at the surface as the nominal composition of the sample. For Mn44, an enrichment of Mn is observed, which suggests that the Mn-oxides present in this sample tend to segregate toward the surface of the electrode.

The effect of Mn addition on the morphology of the anodes was investigated by means of Field-Emission Scanning Electron Microscopy (FESEM). The images at low magnification (Fig. S3) give an idea of how manganese modifies the surface morphology. In Fig. 3, micrographs acquired both in SE (secondary electrons) and BSE (backscattered secondary electrons) are reported for all the investigated samples. TiO_2-RuO_2 anodes exhibit a mud-cracked morphology (Fig. S3a), well-known for this kind of materials [45,54,61,62] and ascribed to the tensile stress induced by the applied thermal treatment [54,62]. Indeed, Mn00 and Mn09 (Figs. S3a, b and 3 a,b) show a similar morphology, with a lower degree of roughness and fewer fractures on the outermost layer. In Mn09, a slight increase of the roughness can be seen compared to Mn00. By taking advantage of the compositional contrast arising from the BSE, it is possible to get an impression of the ruthenium dispersion (*i.e.*, Ru has a higher atomic number than both Ti and Mn). Ruthenium-rich particles are observed both on the plain surface and in the cracks of the electrode (Fig. 3f, g). This is in agreement with EDX elemental mapping of the sample Mn00 (Fig. S4); for this reason, all other samples are discussed referring to micrographs acquired using the BSE detector.

The sample morphology drastically changes when the Mn content is further increased (Mn33, Mn44, and Mn60): the structures become rougher and more porous (Fig. S3c, d, e). In sample Mn33, some porous areas with smaller and more irregular cracks than observed for Mn00 and Mn09 are interconnected by a three-dimensional network of "sunflower"-like structures (Fig. 3c). By looking at the compositional contrast (Fig. 3h), the sample appears quite homogeneous and Ru-rich particles disappear. This suggests that the cracks observed for the first two samples, Mn00 and Mn09, are mainly due to the crystalline growth and slight segregation of RuO_2 particles. This effect is not observed for Mn33 sample, partially because of the reduced loading of ruthenium. A similar effect is found for samples Mn44 and Mn60 (Fig. 3d,e): in these two samples, the porous surface of the electrodes presents some craters. Sample Mn60 also exhibits deep fractures of the film and a homogeneous Ru dispersion (Fig. 3i,j), with a slight enrichment in Ru mainly in the rims of the circular craters.

The porous structure of samples Mn33, Mn44, Mn60, with bubble-like features, is most likely due to differences in surface tension of the Mn-containing solution, a parameter that is well known to influence the morphology of the final material in DSA® anodes by changing the rate of evaporation [34]. The addition of Mn chloride can alter the surface tension of the solution, promoting the formation of bubbles due to released gases during precursor decomposition.

3.2. Electrochemical characterization

The catalytic activity was assessed by linear sweep voltammetry (LSV) at a scan rate of 0.5 mV s^{-1} (Fig. 4a). This low scan rate was chosen to minimize the amount of current generated by the capacitive effect and in order to obtain the corresponding Tafel plots reported in Fig. 4b. The bare titanium substrate exhibits negligible current densities in all potential ranges applied in this work (Fig. S1a, b), and thus its contribution to the catalytic activity for OER can be ignored.

The addition of manganese led to a significant cathodic shift of the voltammograms. Already the sample with the lowest Mn content (Mn09) showed a significant increase in the recorded current density compared to the Mn-free sample (Fig. 4 and Table 2). This sample is also more active than a pure RuO_2 sample prepared with the same method. For samples Mn33, Mn44, and Mn60, a further increase of the catalytic activity is observed. Before, it has been shown that the inclusion of Mn in the RuO_2 lattice enhanced the catalytic activity of $Ru_xMn_{1-x}O_2$ anodes in water oxidation under acidic conditions and the synergy was most pronounced for x = 0.30 [49]. We demonstrate in this work that Mn also promotes the electrocatalytic performance of TiO_2-RuO_2 mixed anodes. Even though at higher content Mn addition leads to segregation of Mn-oxides, this is not detrimental to the synergistic effect between Mn and these dimensionally stabilized TiO_2-RuO_2 anodes.

To confirm that the increased activity is due to a synergistic effect between Mn and Ru and not to Mn itself, we evaluated the activity of a Ru-free sample prepared from a solution containing 70% titanium and 30% manganese precursors (Ti0.7Mn0.3). This sample showed negligible current densities compared to those recorded for Ru-containing samples (Figure S5).

The performance of the electrodes was evaluated from the overpotential (η) required to reach a current density of 1 mA cm^{-2} or 10 mA cm^{-2}. Clearly, η was significantly lowered, nearly proportionally with the Mn loading (Table 2 and Fig. 5). The lowest overpotential at j = 10 mA cm^{-2} is observed for the Mn44 electrode (η = 386 mV). Its overpotential (386 mV) is only 26 mV higher than the overpotential reported for a thin film of pure RuO_2 in 0.05 M H_2SO_4 [63], and 46 mV higher than the value reported for an IrO_x catalyst in 1 M H_2SO_4 [8]. We stress the promising performance of sample Mn44 prepared in a simple procedure, whose activity is comparable to that of pure ruthenium- or iridium-based systems. The benefit of our composition is that the noble metal content is considerably lower. We highlight that this sample, containing only 17 at% Ru, reaches the target of activity designated to highly promising catalysts (η_{10} < 400 mV) in an acidic electrolyte [64].

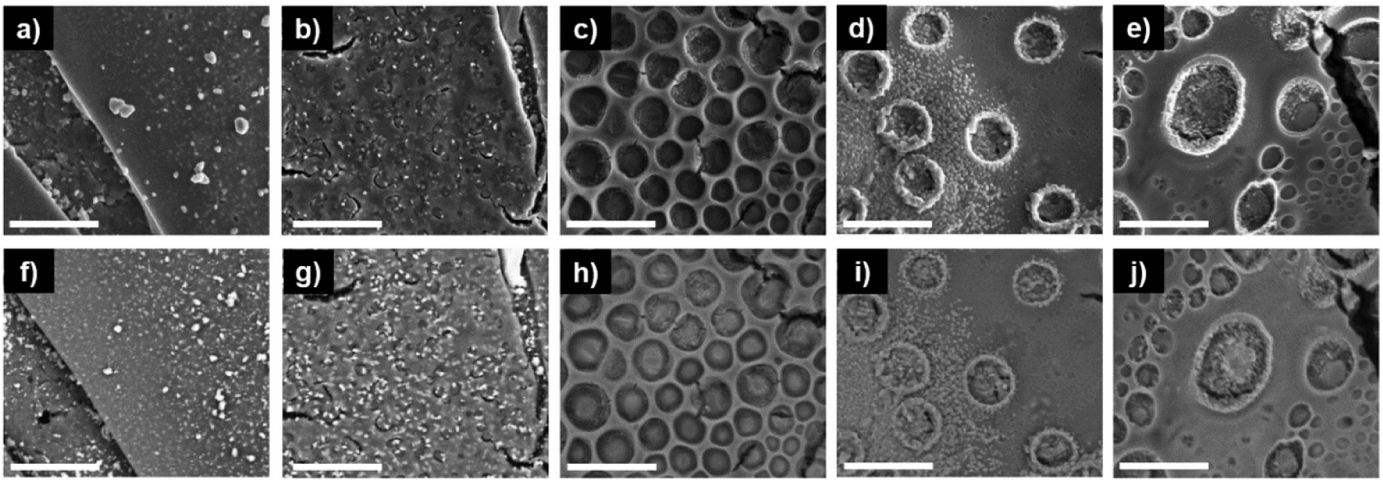

Fig. 3. Electron micrographs acquired in normal detection mode using secondary electrons (top) and back-scattered electron (BSE) mode (bottom) of samples: a, f) Mn00; b, g) Mn09; c, h) Mn33; d, i) Mn44; e, j) Mn60. Scale bars are 2 µm.

We also determined Tafel slopes for the different samples. Tafel slopes for Mn09 and Mn33 are only slightly higher (44–56 mV dec^{-1}) than for Mn00. Only sample Mn60 exhibited a slope higher than 60 mV dec^{-1}. Mn44 exhibited a Tafel slope of 50 mV dec^{-1}, close to the value determined for Mn00 (44 mV dec^{-1}). The changes in the Tafel slopes are indicative of different reaction mechanisms. While Tafel slopes of about 40 mV dec^{-1} are typical for a second electron transfer being the rate-determining step of the reaction, values of about 60 mV dec^{-1} indicate that a chemical step is taking place before the OER [65]. For the sample Mn60, we speculate that electro-oxidation of Mn^{2+} as a chemical step prior to oxygen evolution, as already identified as the rate-determining step in pure MnO_x-catalyzed water oxidation at pH < 8 [25].

The value of the Tafel slope of sample Mn44 of 50 mV dec^{-1} is in line with values reported for Ru-based OER catalysts, *i.e.* in the 30–60 mV dec^{-1} range [66,67], and lower than the Tafel slopes reported for Ir-based catalysts (typically 55–65 mV dec^{-1} range) [68,69].

As the very different morphologies of the films can influence the current densities exposing more active sites, we also determined the electrochemical surface area (ECSA). Higher surface areas contribute to higher the observed current densities [70]; it is therefore relevant to normalize the results based on the ECSA to gain insights into the intrinsic activity. The normalization with the geometric area only does not allow to distinguish whether an activity change is caused by extrinsic (different surface areas) or intrinsic factors ("real" electrocatalysis). The ECSA was evaluated from the ratio between the double-layer capacitance obtained by EIS and the specific capacitance of metal oxides in acidic electrolytes (35 µF cm^{-2}), following the approach described by McCrory et al. [27] We refer to their work for the explanation of the assumptions and accuracy of the method [27]. As follows from Table 2, the ECSA substantially increases when the Mn content is raised. The effect on the ECSA is most pronounced when the Mn content is increased from 0 to 33 at%. The nearly one order of magnitude increase shows a strong textural influence of Mn on the catalytic performance. The ECSA differences are in qualitative agreement with the FESEM images.

Table 2
Summary of overpotentials at 1 and 10 mA cm^{-2}*geo* (η1, η10), Tafel slopes, ECSA values, and specific current densities at an overpotential of 300 mV normalized with ECSA (j_{spec}, η = 300 mV).

Sample ID	η_1, mV	η_{10}, mV	Tafel slope, mV dec^{-1}	ECSA, cm^2	$j_{spec,\ \eta=300\ mV}$, µA cm^{-2}_{ECSA}
Mn00	404	609	44	54	1.31
Mn09	338	448	50	180	1.65
Mn33	290	416	56	497	2.78
Mn44	273	386	50	594	3.85
Mn60	268	402	61	669	3.51

However, even after normalization of the Tafel plots with the values of the ECSA instead of the geometric areas (Fig. 4c), we can still observe a shift of the curves towards higher current densities. In particular, the trend in the low overpotential region is similar to the trend observed for the current densities normalized with the geometric area, where the catalytic activity increases with the Mn content. This finding shows that a higher content also affects the intrinsic activity of the anodes. In the high overpotential region, the sample with the highest intrinsic activity

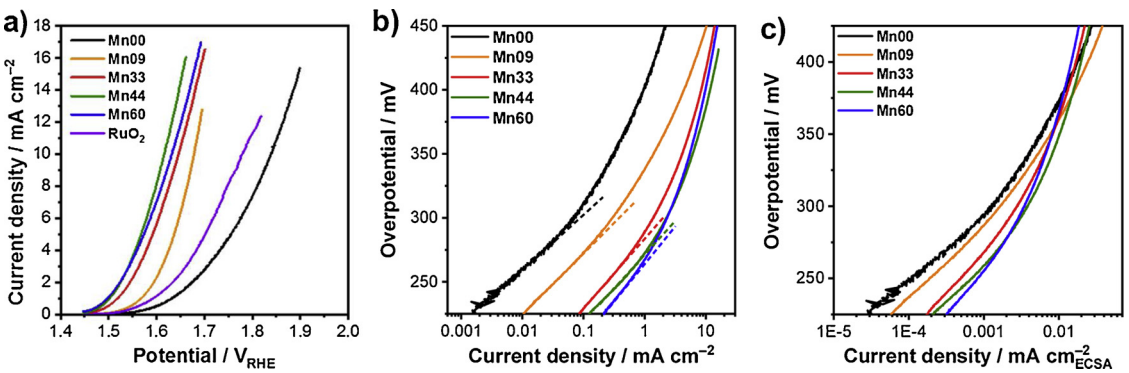

Fig. 4. a) Linear sweep voltammetries and b) corresponding Tafel plots of the anodes recorded in 0.1 M H_2SO_4. Linear Tafel regions are indicated by dashed lines. c) Tafel plots of the electrodes normalized with ECSA.

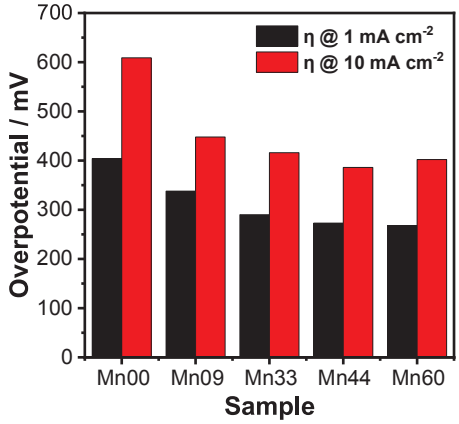

Fig. 5. Overpotentials of mixed TiO_2-RuO_2-MnO_x anodes required to reach current densities of 1 mA cm^{-2} and 10 mA cm^{-2} determined by LSV in a 0.1 M H_2SO_4 solution at 25 °C. Current densities are normalized on the geometric areas of the electrodes.

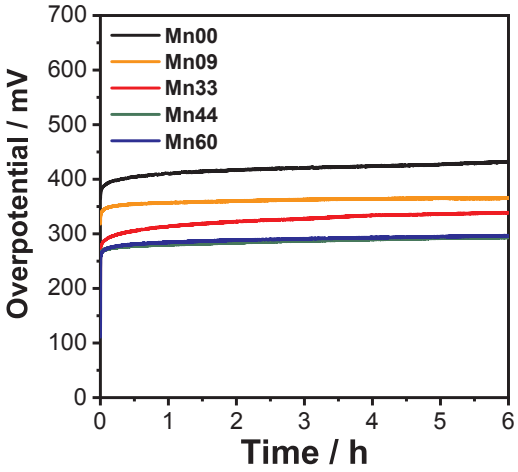

Fig. 6. Chronopotentiometries of mixed TiO_2-RuO_2-MnO_x anodes recorded in 0.1 M H_2SO_4 at a constant current density of 1 mA cm^{-2}.

is Mn09. This may find its origin in the mass transport limitations for the samples Mn33, Mn44 and Mn60 by vigorous oxygen bubble formation at the surface.

In Table 2 we evaluated the specific current densities normalized with the values of ECSA for all the samples at a fixed overpotential of 300 mV. The results show an increase of the specific activity upon Mn addition up to sample Mn44, which displayed the best performance. The recorded specific current density for sample Mn44 (3.85 μA cm^{-2}_{ECSA}) is substantially higher compared to Mn00 (1.31 μA cm^{-2}_{ECSA}). A further increase in Mn content did not yield to a further increase in the specific activity.

To the best of our knowledge, no ECSA-normalized results of the catalytic performances of similar systems (*i.e.*, RuO_2 –MnO_x) have been previously reported. Thus, our findings show that, in addition to the positive influence of manganese on the dispersion of Ru, there is also a qualitative influence of the Mn promoter on the Ru active sites. The activity enhancement can be due to the presence of defects in the rutile structure resulting from Mn insertion into the TiO_2-RuO_2 solid solution, as observed by XRD. The presence of disordered surface structures can lead to increased OER performance, because the higher density of unsaturated sites enhances reactant adsorption and the higher structural flexibility of the active sites stabilizes the formation of intermediates. This is for instance observed for RuO_2, the amorphous form exhibiting a higher OER activity than its crystalline counterpart [71]. The enhanced activity of catalysts with a high number of oxygen vacancies finds origin in the participation of lattice oxygen atoms in the oxygen evolution, which is also the reason of the higher dissolution rates usually recorded for these materials [72].

The stability of the catalysts was evaluated by chronopotentiometry (CP) conducted for 6 h in 0.1 M H_2SO_4 at a current density of 1 mA cm^{-2}. The addition of Mn not only results in increased electrocatalytic activity but also in improved stability (Fig. 6). This improved stability is already evident at a Mn content of 9 at%. The overpotential remains nearly constant during the CP measurement, in contrast to sample Mn00. Sample Mn33 shows an increase in the overpotential during time, yet still exhibiting lower values at the end of the test compared to the samples with a lower Mn content. We ascribe the increase of overpotential for this sample to its three-dimensional porous structure, which is substantially altered during the electrochemical treatment, as will be shown below. Sample Mn44 is not only the most active sample but also displays the highest stability, *i.e.* the overpotential remains below 300 mV after 6 h. A similar value was recorded for the sample with the highest Mn content (Mn60).

3.3. Effect of electrochemical treatment on the electrodes

The influence of a prolonged electrochemical treatment on the electrode morphology was analyzed by means of FESEM. Micrographs of the anodes at high magnification are reported for all the samples in Fig. 7 (micrographs at low magnification in Fig. S3). The morphology of samples with no Mn or a low Mn content (Mn00 and Mn09) does not substantially change upon electrochemical treatment (Fig. S3f, g, and Fig. 7a, b, f, g). Mostly, a flattening of the surface and a reduced number of cracks are noticed. A severe morphology change is visible for sample Mn33, which can explain the substantial change in performance during the treatment. The ordered and porous structure characterizing the fresh sample Mn33 is unstable under OER conditions, as it is converted and replaced by a disordered and rougher structure (Figs. S3 h and 7 c, h) after the electrochemical treatment. The samples with a high Mn content (Mn44 and Mn60) maintain a morphology with craters (Figs. S3i,j and 7 d, e) with a homogenous dispersion of the elements (Fig. 7i, j).

X-ray diffractograms of the tested samples (Fig. S6) show for all the samples a decrease in peak intensities, which is an evidence of a lowered crystallinity of the electrodes due to the electrochemical treatment. The sharp peaks originating from the Mn-oxides observed in fresh Mn44 and Mn60 samples are absent in the spectra of the used anodes. Thus, the electrochemical treatment causes a substantial decrease in the crystallinity and, possibly, leaching of Mn from the anode surface. As the overpotential at the end of the stability tests remains lower for the Mn samples from which crystalline Mn-oxides were removed, it is likely that their higher catalytic activity originates from the inclusion of Mn in the lattice of the mixed TiO_2-RuO_2 rutile phase and the porous structure with a better Ru dispersion.

XPS results (Table S2) show that the Mn content of sample Mn44 at the surface dramatically decreased from 71 at% in the fresh sample to 17 at% after electrochemical treatment. The peak splitting of the samples with a higher Mn content decreased significantly (Fig. S2b, Table S1). From the values for the used catalysts, we infer that the remaining Mn is mainly present as Mn(IV) [56–58], likely as a substituent in the TiO_2-RuO_2 lattice. The Mn(II) and Mn(III) species present in the fresh samples as segregated oxides were further oxidized during electrochemical oxidation and eventually dissolved in the solution as MnO_4^- [73]. The aspect of stability is further investigated in the remainder of this work. Based on the activity and stability results, we selected sample Mn44 for these further investigations, because this sample had the lowest overpotential at a current density of 10 mA cm^{-2} during the LSV, the lowest overpotential at the end of the chronopotentiometry, lower Tafel slope compared to Mn60, and the highest

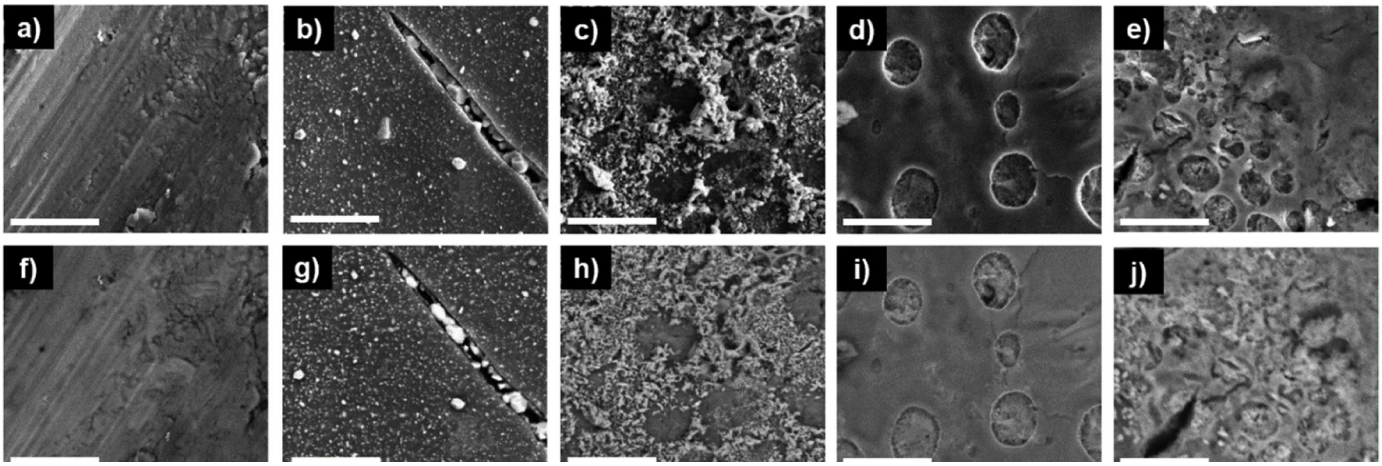

Fig. 7. Electron micrographs acquired in normal detection mode using secondary electrons (top) and back-scattered electron (BSE) mode (bottom) of samples after 6 h of electrolysis at 1 mA cm^{-2} in 0.1 M H_2SO_4: a, f) Mn00; b, g) Mn09; c, h) Mn33; d, i) Mn44; e, j) Mn60. Scale bars are 2 µm.

specific current density at an overpotential of 300 mV.

3.4. Online electrochemical mass spectrometry (OLEMS)

In contrast to conventional electrochemical analysis, OLEMS provides semi-quantitative information on the gases evolving at the electrode. A low detection limit and fast response enable instantaneous detection of reaction products during dynamic electrochemical treatment. We employed OLEMS to determine the OER onset potentials for samples Mn00 and Mn44 by measuring the O_2 signal as a function of the applied potential (Fig. 8a, b). Surprisingly, the onset potentials of the O_2 production were nearly similar for these two samples, *i.e.*, 250 ± 10 mV and 260 ± 10 mV, respectively. Although this seems to be in disagreement with the overpotentials reported in Table 2, we suspect that, at this initial stage, a part of the charge is used to oxidize Mn, as we will discuss below.

OLEMS can also be used for studying competitive reactions by means of Faraday plots [52]. In Fig. S7 we report the three-dimensional representations of the gas production *versus* potential applied and charge for both the samples Mn00 and Mn44. The projections in two dimensions of the gas productions *versus* the charge result in the Faraday plots, reported in Fig. 8c, d.

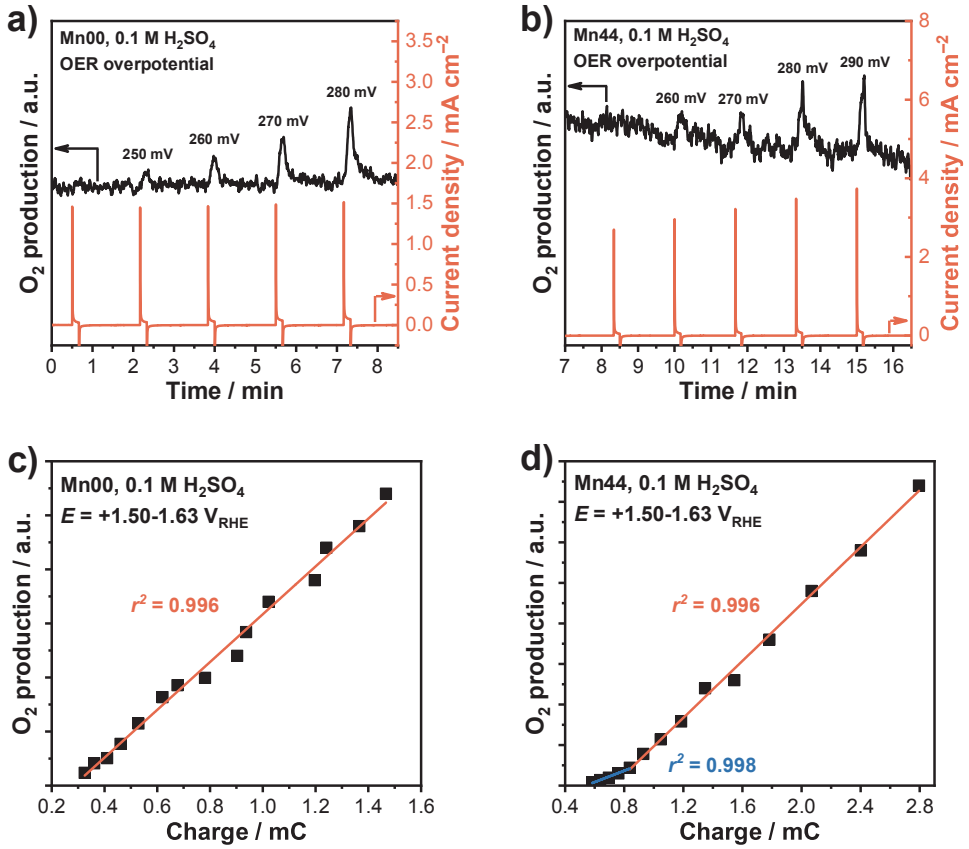

Fig. 8. Potential-dependent O_2^+ (m/z = 32) ion currents of a) Mn00 and b) Mn44 samples recorded at low overpotential values (η > 240 mV); corresponding Faraday plots of c) Mn00 and d) Mn44 recorded at E = . 1.50–1.63 V.

Faraday plots represent the potential dependence of the amount of product formed per amount of supplied faradaic charge, in accordance with the Faraday's law of electrolysis. Linearity between the gas production and faradaic charge is expected for systems where only a single faradaic reaction occurs in the studied potential range. Deviations can occur when more than one faradaic reaction is involved.

Fig. 8c shows a linear behavior of O_2 production against faradaic charge for sample Mn00, suggesting that the OER is the major electrochemical reaction occurring at $E = +1.50 \div 1.63$ V. On the contrary, a Faraday plot for sample Mn44 exhibits two distinct regions in $E_1 = +1.50 \div 1.54$ V and $E_2 = +1.54 \div 1.63$ V with different slopes (Fig. 8d). The lower slope in region E_1 compared to region E_2 indicates that part of the charge is used for another reaction than the OER. Considering the Pourbaix diagram of Mn in water, [74] we surmise that, at E_1, part of the charge is consumed to oxidize Mn^{2+} and Mn^{3+} to Mn(IV) and Mn(VII) in accordance with XPS analysis (Fig. S2 and Table S1). The formation of MnO_4^- leads to partial dissolution of Mn into the electrolyte [25].

During the OLEMS experiment, we also monitored the signal of the fragment $m/z = 34$ ($H_2O_2^+$). At the highest potential applied in our experiment (E = 1.63 V_{RHE}, *i.e.* $\eta_{OER} = 400$ mV), this signal accounted for 0.4 ± 0.2% of the sum between O_2^+ and $H_2O_2^+$ for both Mn00 and Mn44. However, as the thermodynamic potential of the oxidation of water to H_2O_2 is +1.77 V_{RHE}, the formation of H_2O_2 has to be ascribed to the recombination of molecular H_2 and O_2 present in the solution [75].

3.5. Stability evaluation: XPS depth profiles and ICP-OES

To compare the stability of sample Mn44 with sample Mn00 under more severe conditions, we subjected the two samples to a constant electrolysis at $E = +1.8$ V_{RHE} for 17 h. These tests aimed to provide insights about the structural modifications occurring to the anodes during prolonged electrolysis. The chronoamperograms (Fig. S8) show a significant decrease of the current density for the sample Mn44 at the beginning of the test. After this rapid decrease, the current density stabilizes and even after 17 h the recorded current density remains higher than for Mn00. To better understand the degradation process occurring during long-term electrolysis, we performed XPS depth profiling for fresh samples and those subjected to 3 h or 17 h electrolysis at $E = +1.8$ V_{RHE}.

XPS depth profiling analysis comprises cycles of high-energy ion sputtering alternated with XPS measurements. The sputtering time is proportional to the thickness of the layer removed during a sputtering cycle. As a direct correlation between sputtering time and thickness can only be obtained for systems with known sputtering constants, the thickness of the analyzed sample is usually only given in terms of sputtering times. Fig. 9 shows XPS depth profiles for Mn00 and Mn44 before and after electrolysis for 3 and 17 h (more data in Fig. S9). The changes in the depth profiles were more pronounced for Mn44 than for Mn00. For Mn44, leaching of Ru- and Mn-oxides is pronounced after 3 h with only limited changes after further electrolysis. From this, we conclude that the EC-induced dissolution of RuO_2 occurs mostly at the initial stage of electrolysis, in keeping with literature [76–78]. Mn leaching is much more severe than Ru leaching, indicative of the lower stability of the former in the film. The thickness of the films can be semi-quantitatively evaluated from the sputtering times needed to remove Ru and obtain the pure Ti^0 substrate signal. Clearly, this sputtering time is much longer for Mn44 ($t_s \approx 3.5$ h) than for Mn00 ($t_s \approx 2$ h), confirming that Mn addition increases the thickness of the film by modifying its morphology.

We also measured the elemental composition of the used electrolytes by ICP-OES after 17 h electrolysis (Table 3).

The potential applied in the chronoamperometry is higher than the thermodynamic potentials of Ru and Mn dissolution. Ru anodic dissolution involves the formation of RuO_4 thorough the following reaction:

$$RuO_2 + 2H_2O \rightarrow RuO_4 + 4H^+ + 4e^- \quad (2)$$

The formation of RuO_4 has a thermodynamic potential of 1.387 V_{SHE} [36,79] and its onset is typically observed close to the OER onset [80,81].

The dissolution of Mn_2O_3 and Mn_3O_4 in H_2SO_4 includes the formation of an oxyhydroxide [82], which undergoes disproportionation through the following reaction:

$$2MnOOH + 2H^+ \rightarrow MnO_2 + Mn^{2+} + 2H_2O \quad (3)$$

At potentials higher than 1.7 V_{RHE}, MnO_2 is oxidized to MnO_4^- through the following reaction:

$$MnO_2 + 2H_2O \rightarrow MnO_4^- + 4H^+ + 3e^- \quad (4)$$

The amount of dissolved metals and the dissolution rates normalized to the geometric surface area listed in Table 3 confirms that leaching of Ru, Mn and Ti is more pronounced for Mn44 than for Mn00. This higher dissolution rate can derive from the approximately one-order of magnitude higher ECSA of Mn44 in comparison to Mn00. The ruthenium dissolution rate for sample Mn44 (5.04 nmol cm^{-2} h^{-1}), even though higher than for sample Mn00, is lower than what previously reported for pure RuO_2 [63]. This implies that this novel anode composition presents an increased activity compared to standard DSA®, still benefiting from the stabilizing effect of TiO_2.

To take into account the different electrochemical surface areas exposed, we normalized the dissolution rates to the ECSA. The resulting data also given in Table 3 show that the surface-normalized Ru dissolution rate in Mn44 (0.008 nmol h^{-1} cm_{ECSA}^{-2}) is two times lower than in Mn00 (0.019 nmol h^{-1} cm_{ECSA}^{-2}). However, as the Ru content in the Mn00 is twice that in Mn44, we conclude that the dissolution rates are nearly similar.

The Ti dissolution rate is higher for Mn44 than for Mn00, which is most likely due to the more extensive exposure of the Ti substrate in the more open Mn-containing film. Therefore, we infer from these data that dissolution of Ru is mainly more severe in the porous film due to the higher surface area and also that Mn does not influence the intrinsic stability of the films.

The elemental analysis results obtained by ICP-OES can be used to calculate the charge spent in metal dissolution processes by applying Faraday's law and to derive the Faradic efficiencies of these reactions. Assuming that (2) and (4) are the oxidation reactions of ruthenium and manganese in sample Mn44, the Faradaic efficiencies of the dissolution of ruthenium and manganese are 0.007% and 0.025%. These extremely low values, in combination with the low selectivity of H_2O_2 measured by OLEMS (0.4 ± 0.2%), led us to conclude that OER is the main reaction taking place at the anode.

4. Conclusions

In this work, we synthesized mixed TiO_2-RuO_2 electrodes for acidic water electrolysis by a sol-gel method and investigated the influence of Mn addition on the structure, morphology, activity, and stability of the electrodes for the oxygen evolution reaction. The presence of Mn in the preparation led to a more open structure of the mixed oxide film, evident from a strong increase of the electrochemical surface area. Surface-area corrected current densities suggest that Mn inclusion in the film results in a higher intrinsic electrochemical activity of the mixed oxide compared to TiO_2-RuO_2. Detailed characterization shows that Mn is predominantly inserted into the rutile phase, while the segregation of Mn-oxides is evident at higher Mn content. The most active sample contains 44 at% Mn and reaches an overpotential of 386 mV at a current density at 10 mA cm^{-2}, and proved to be stable during electrolysis for 6 h. Its Tafel slope was 50 mV dec^{-1}, close to the value recorded for Mn00 (44 mV dec^{-1}). This performance is high considering that the

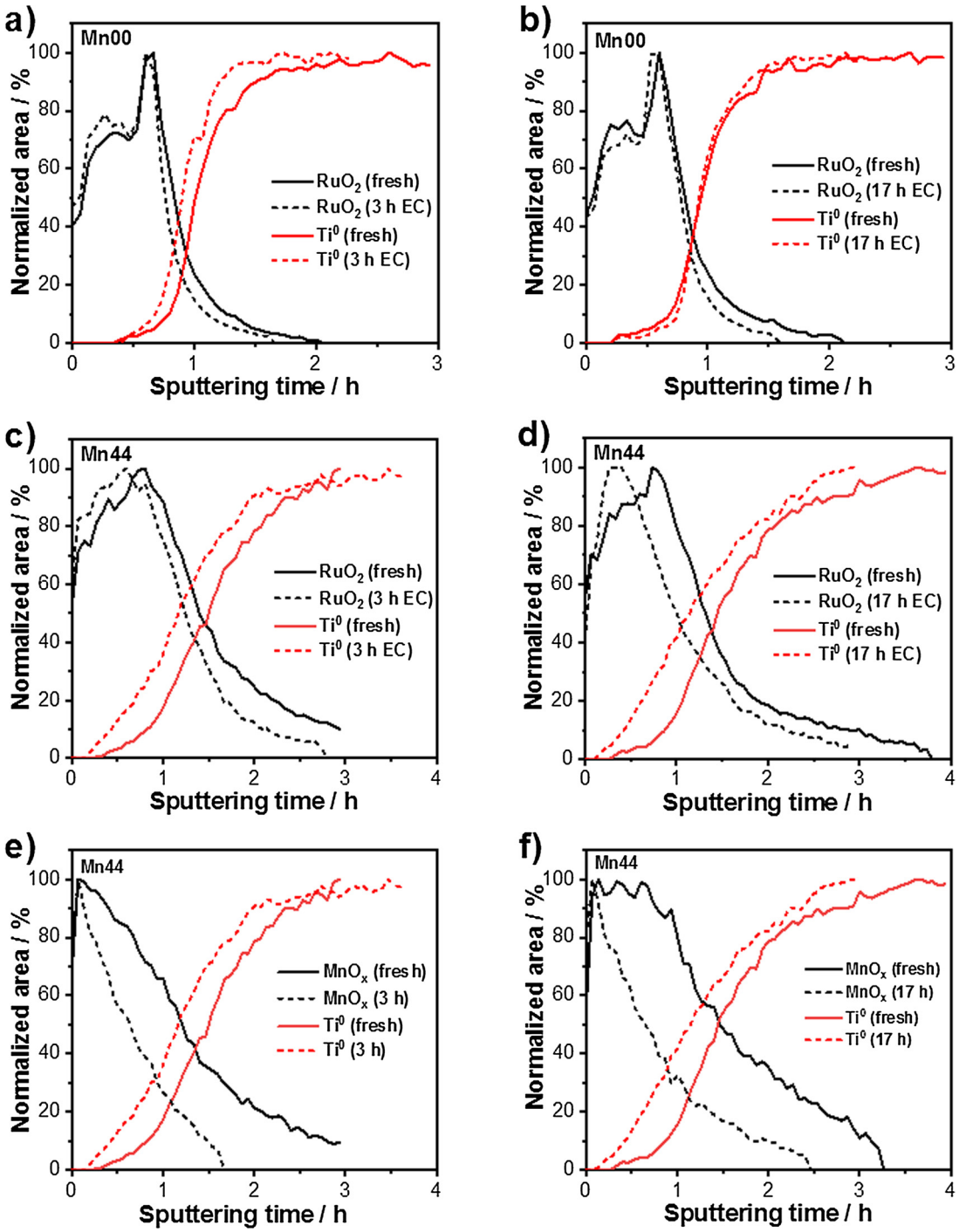

Fig. 9. XPS depth profiles of a, b) Mn00 and: c, d, e, f) Mn44 subjected to $E = 1.8\ V_{RHE}$ in 0.1 M H_2SO_4 for 3 h (a, c, e) and 17 h (b, d, f).

catalyst was obtained by a simple preparation method and the final film only contained 17 at% Ru. The presence of Mn not only contributes to boosting the electrochemical OER performance of TiO_2-RuO_2 but, at the same time, drastically decreases the precious metal content and thus the price of the anodes. As the segregated Mn-oxides are removed during long-term electrolysis, it is reasonable to conclude that the synergistic effect is due to the inclusion of Mn in mixed TiO_2-RuO_2 anodes. Detailed analysis of the anode surface during long-term electrolysis shows that Ru dissolution is higher in the more porous Mn-promoted film than for the TiO_2-RuO_2 one. Normalization of dissolution rates suggests that the intrinsic dissolution rate of Ru is independent of the morphology and also does not depend on the presence of Mn.

Declaration of Competing Interest

The authors declare that they have no known competing financial interests or personal relationships that could have appeared to influence the work reported in this paper.

Acknowledgments

The authors would like to thank Adelheid Elemans-Mehring of Eindhoven University of Technology for ICP-OES measurements. M.E.C.P. acknowledges funding by a Graduate School program from the Netherlands Organization for Scientific Research (NWO). A.G. and

Table 3
Amount of metals dissolved during 17 h of constant electrolysis at E = 1.8 V_{RHE} and leaching rates normalized with ECSA (metal content determined by ICP-OES elemental analysis).

	Mn00	Mn44
Ru, nmol cm^{-2}	17.8 ± 0.4	85.6 ± 0.5
Mn, nmol cm^{-2}	n/a	412 ± 1
Ti, nmol cm^{-2}	42.1 ± 0.1	711.1 ± 0.9x
Ru, nmol h^{-1} cm^{-2}	1.05 ± 0.02	5.04 ± 0.03
Mn, nmol h^{-1} cm^{-2}	n/a	24.26 ± 0.07
Ti, nmol h^{-1} cm^{-2}	2.47 ± 0.01	41.83 ± 0.1
Ru, nmol h^{-1} cm^{-2} $_{ECSA}$	0.019 ± 0.001	0.008 ± 0.001
Mn, nmol h^{-1} cm^{-2} $_{ECSA}$	n/a	0.041 ± 0.001
Ti, nmol h^{-1} cm^{-2} $_{ECSA}$	0.046 ± 0.001	0.070 ± 0.001

E.J.M.H. acknowledge funding from a NWO Vici grant.

Appendix A. Supplementary data

Supplementary material related to this article can be found, in the online version, at doi:https://doi.org/10.1016/j.apcatb.2019.118225.

References

[1] D.G. Nocera, N.S. Lewis, Powering the planet: chemical challenges in solar energy utilization, Proc. Natl. Acad. Sci. U. S. A. 103 (2006) 15729–15735, https://doi.org/10.1073/pnas.0603395103.

[2] S.Y. Reece, Ja. Hamel, K. Sung, T.D. Jarvi, a.J. Esswein, J.J.H. Pijpers, D.G. Nocera, Wireless solar water splitting using silicon-based semiconductors and earth-abundant catalysts, Science (334) (2011) 645–648, https://doi.org/10.1126/science.1209816.

[3] C.R. Cox, J.Z. Lee, D.G. Nocera, T. Buonassisi, Ten-percent solar-to-fuel conversion with nonprecious materials, Proc. Natl. Acad. Sci. 111 (2014) 14057–14061, https://doi.org/10.1073/pnas.1414290111.

[4] J. Luo, J.H. Im, M.T. Mayer, M. Schreier, M.K. Nazeeruddin, N.G. Park, S.D. Tilley, H.J. Fan, M. Grätzel, Water photolysis at 12.3% efficiency via perovskite photovoltaics and Earth-abundant catalysts, Science (345) (2014) 1593–1596, https://doi.org/10.1126/science.1258307.

[5] H. Ibrahim, A. Ilinca, J. Perron, Energy storage systems—characteristics and comparisons, Renewable Sustainable Energy Rev. 12 (2008) 1221–1250, https://doi.org/10.1016/j.rser.2007.01.023.

[6] N.-T. Suen, S.-F. Hung, Q. Quan, N. Zhang, Y.-J. Xu, H.M. Chen, Electrocatalysis for the oxygen evolution reaction: recent development and future perspectives, Chem. Soc. Rev. 46 (2017) 337–365, https://doi.org/10.1039/C6CS00328A.

[7] R.F. Scarr, The mechanism of oxygen evolution on nickel, platinum, and other metals and alloys, J. Electrochem. Soc. 116 (1969) 1526, https://doi.org/10.1149/1.2411597.

[8] C.C.L. McCrory, S. Jung, I.M. Ferrer, S.M. Chatman, J.C. Peters, T.F. Jaramillo, Benchmarking HER and OER electrocatalysts for solar water splitting devices, J. Am. Chem. Soc. 137 (2015) 4347–4357, https://doi.org/10.1021/ja510442p.

[9] M. Yagi, M. Kaneko, Molecular catalysts for water oxidation, Chem. Rev. 101 (2001) 21–35, https://doi.org/10.1021/cr980108l.

[10] I. Roger, M.A. Shipman, M.D. Symes, Earth-abundant catalysts for electrochemical and photoelectrochemical water splitting, Int. Rev. Chem. Eng. 1 (2017) 1–13, https://doi.org/10.1038/s41570-016-0003.

[11] M.S. Burke, L.J. Enman, A.S. Batchellor, S. Zou, S.W. Boettcher, Oxygen evolution reaction electrocatalysis on transition metal oxides and (Oxy)hydroxides: activity trends and design principles, Chem. Mater. 27 (2015) 7549–7558, https://doi.org/10.1021/acs.chemmater.5b03148.

[12] M. Gong, H. Dai, A mini review of NiFe-based materials as highly active oxygen evolution reaction electrocatalysts, Nano Res. 8 (2014) 23–39, https://doi.org/10.1007/s12274-014-0591-z.

[13] X. Li, F.C. Walsh, D. Pletcher, Nickel based electrocatalysts for oxygen evolution in high current density, alkaline water electrolysers, Phys. Chem. Chem. Phys. 13 (2011) 1162–1167, https://doi.org/10.1039/c0cp00993h.

[14] M. Gong, Y. Li, H. Wang, Y. Liang, J.Z. Wu, J. Zhou, J. Wang, T. Regier, F. Wei, H. Dai, An advanced Ni–Fe layered double hydroxide electrocatalyst for water oxidation, D J. Am. Chem. Soc. (2013) 2–5, https://doi.org/10.1021/ja4027715.

[15] M. Gao, W. Sheng, Z. Zhuang, Q. Fang, S. Gu, J. Jiang, Y. Yan, Efficient water oxidation using nanostructured α-nickel-hydroxide as an electrocatalyst, J. Am. Chem. Soc. 136 (2014) 7077–7084, https://doi.org/10.1021/ja502128j.

[16] X. Lu, C. Zhao, Electrodeposition of hierarchically structured three-dimensional nickel–iron electrodes for efficient oxygen evolution at high current densities, Nat. Commun. 6 (2015) 1–7, https://doi.org/10.1038/ncomms7616.

[17] X. Deng, H. Tuysuz, Cobalt-oxide-Based materials as water oxidation catalyst: recent progress and challenges, ACS Catal. 4 (2014) 3701–3714, https://doi.org/10.1021/cs500713d.

[18] M.W. Kanan, D.G. Nocera, In situ formation of an oxygen-evolving catalyst in neutral water containing phosphate and Co^{2+}, Science (321) (2008) 1072–1075, https://doi.org/10.1126/science.1162018.

[19] Y. Surendranath, M.W. Kanan, D.G. Nocera, Mechanistic studies of the oxygen evolution reaction by a cobalt-phosphate catalyst at neutral pH, J. Am. Chem. Soc. 132 (2010) 16501–16509, https://doi.org/10.1021/ja908730h.(45).

[20] A.J. Esswein, Y. Surendranath, S.Y. Reece, D.G. Nocera, Highly active cobalt phosphate and borate based oxygen evolving catalysts operating in neutral and natural waters, Energy Environ. Sci. 4 (2011) 499–504, https://doi.org/10.1039/C0EE00518E.

[21] Y. Surendranath, D.A. Lutterman, Y. Liu, D.G. Nocera, Nucleation, growth, and repair of a cobalt-based oxygen evolving catalyst, J. Am. Chem. Soc. 134 (2012) 6326–6336, https://doi.org/10.1021/ja3000084.

[22] I. Zaharieva, P. Chernev, M. Risch, K. Klingan, M. Kohlhoff, A. Fischer, H. Dau, Electrosynthesis, functional, and structural characterization of a water-oxidizing manganese oxide, Energy Environ. Sci. 5 (2012) 7081–7089, https://doi.org/10.1039/C2EE21191B.

[23] A. Bergmann, I. Zaharieva, H. Dau, P. Strasser, Electrochemical water splitting by layered and 3D cross-linked manganese oxides: correlating structural motifs and catalytic activity, Energy Environ. Sci. 6 (2013) 2745–2755, https://doi.org/10.1039/c3ee41194j.

[24] M. Huynh, C. Shi, S.J.L. Billinge, D.G. Nocera, Nature of activated manganese oxide for oxygen evolution, J. Am. Chem. Soc. 137 (2015) 14887–14904, https://doi.org/10.1021/jacs.5b06382.

[25] T. Takashima, K. Hashimoto, R. Nakamura, Mechanisms of pH-dependent activity for water oxidation to molecular oxygen by MnO_2 electrocatalysts, J. Am. Chem. Soc. 134 (2012) 1519–1527, https://doi.org/10.1021/ja206511w.

[26] M. Etzi Coller Pascuzzi, E. Selinger, A. Sacco, M. Castellino, P. Rivolo, S. Hernández, G. Lopinski, I. Tamblyn, R. Nasi, S. Esposito, M. Manzoli, B. Bonelli, M. Armandi, Beneficial effect of Fe addition on the catalytic activity of electrodeposited MnO_x films in the water oxidation reaction, Electrochim. Acta 284 (2018), https://doi.org/10.1016/j.electacta.2018.07.148.

[27] C.C.L. McCrory, S. Jung, J.C. Peters, T.F. Jaramillo, Benchmarking heterogeneous electrocatalysts for the oxygen evolution reaction, J. Am. Chem. Soc. 135 (2013) 16977–16987, https://doi.org/10.1021/ja407115p.

[28] S. Jung, C.C.L. McCrory, I.M. Ferrer, J.C. Peters, T.F. Jaramillo, Benchmarking nanoparticulate metal oxide electrocatalysts for the alkaline water oxidation reaction, J. Mater. Chem. A Mater. Energy Sustain. 4 (2016) 3068–3076, https://doi.org/10.1039/C5TA07586F.

[29] L. Trotochaud, J.K. Ranney, K.N. Williams, S.W. Boettcher, Solution-cast metal oxide thin film electrocatalysts for oxygen evolution, J. Am. Chem. Soc. 134 (2012) 17253–17261, https://doi.org/10.1021/ja307507a.

[30] M. Carmo, D.L. Fritz, J. Mergel, D. Stolten, A comprehensive review on PEM water electrolysis, Int. J. Hydrogen Energy 38 (2013) 4901–4934, https://doi.org/10.1016/j.ijhydene.2013.01.151.

[31] K.E. Ayers, E.B. Anderson, C. Capuano, B. Carter, L. Dalton, G. Hanlon, J. Manco, M. Niedzwiecki, Research advances towards low cost, high efficiency PEM electrolysis, ECS Trans. (2010) 3–15, https://doi.org/10.1149/1.3484496.

[32] H.B. Beer, The invention and industrial development of metal anodes, J. Electrochem. Soc. 127 (1980) 303C–307C.

[33] S. Trasatti, Electrocatalysis: understanding the success of DSA®, Electrochim. Acta 45 (2000) 2377–2385, https://doi.org/10.1016/S0013-4686(00)00338-8.

[34] C. Comninellis, G.P. Vercesi, Characterization of DSA®-type oxygen evolving electrodes: choice of a coating, J. Appl. Electrochem. 21 (1991) 335–345, https://doi.org/10.1007/BF01020219.

[35] Y. Lee, J. Suntivich, K.J. May, E.E. Perry, Y. Shao-Horn, Synthesis and activities of rutile IrO_2 and RuO_2 nanoparticles for oxygen evolution in acid and alkaline solutions, J. Phys. Chem. Lett. (2012) 399–404, https://doi.org/10.1021/jz2016507.

[36] N. Hodnik, P. Jovanovič, A. Pavlišič, B. Jozinović, M. Zorko, M. Bele, V.S. Šelih, M. Šala, S. Hočevar, M. Gaberšček, New insights into corrosion of ruthenium and ruthenium oxide nanoparticles in acidic media, J. Phys. Chem. C. 119 (2015) 10140–10147, https://doi.org/10.1021/acs.jpcc.5b01832.

[37] T.D. Nguyen, G.G. Scherer, Z.J. Xu, A facile synthesis of size-controllable IrO_2 and RuO_2 nanoparticles for the oxygen evolution reaction, Electrocatalysis 7 (2016) 420–427, https://doi.org/10.1007/s12678-016-0321-2.

[38] E.A. Paoli, F. Masini, R. Frydendal, D. Deiana, C. Schlaup, M. Malizia, T.W. Hansen, S. Horch, I.E.L. Stephens, I. Chorkendorff, Oxygen evolution on well-characterized mass-selected Ru and RuO_2 nanoparticles, Chem. Sci. 6 (2015) 190–196, https://doi.org/10.1039/C4SC02685C.

[39] T. Reier, M. Oezaslan, P. Strasser, Electrocatalytic oxygen evolution reaction (OER) on Ru, Ir, and Pt catalysts: a comparative study of nanoparticles and bulk materials, ACS Catal. 2 (2012) 1765–1772, https://doi.org/10.1021/cs3003098.

[40] K. Macounova, J. Jirkovsky, M. Makarova, J. Franc, P. Krtil, Oxygen evolution on $Ru_{1-x}Ni_xO_{2-y}$ nanocrystalline electrodes, J. Solid State Electrochem. 13 (2009) 959–965, https://doi.org/10.1007/s10008-008-0624-1.

[41] K. Macounová, M. Makarova, J. Jirkovský, J. Franc, P. Krtil, Parallel oxygen and chlorine evolution on $Ru_{1-x}Ni_xO_{2-y}$ nanostructured electrodes, Electrochim. Acta 53 (2008) 6126–6134, https://doi.org/10.1016/j.electacta.2007.11.014.

[42] J. Jirkovský, H. Hoffmannová, M. Klementová, P. Krtil, Particle size dependence of the electrocatalytic activity of nanocrystalline RuO2 electrodes, J. Electrochem. Soc. 153 (2006) E111–E118, https://doi.org/10.1149/1.2189953.

[43] K. Macounová, M. Makarova, J. Franc, J. Jirkovský, P. Krtil, Influence of Oxygen on Reactivity of $Ru_{1-x}Fe_xO_{2-y}$-Doped Materials, Electrochem. Solid-State Lett. 11 (2008) F27, https://doi.org/10.1149/1.2978963.

[44] V. Petrykin, K. MacOunova, J. Franc, O. Shlyakhtin, M. Klementova, S. Mukerjee, P. Krtil, Zn-doped RuO2 electrocatalyts for selective oxygen evolution: relationship between local structure and electrocatalytic behavior in chloride containing media,

Chem. Mater. 23 (2011) 200–207, https://doi.org/10.1021/cm1028782.
[45] M.P. Browne, H. Nolan, G.S. Duesberg, P.E. Colavita, M.E.G. Lyons, Low-over-potential high-activity mixed manganese and ruthenium oxide electrocatalysts for oxygen evolution reaction in alkaline media, ACS Catal. 6 (2016) 2408–2415, https://doi.org/10.1021/acscatal.5b02069.
[46] M.P. Browne, H. Nolan, B. Twamley, G.S. Duesberg, P.E. Colavita, M.E.G. Lyons, Thermally prepared Mn2O3/RuO2/Ru thin films as highly active catalysts for the oxygen evolution reaction in alkaline media, ChemElectroChem. 3 (2016) 1847–1855, https://doi.org/10.1002/celc.201600370.
[47] D. Cipris, D. Pouli, Oxygen evolution on dimensionally stable anode, J. Electroanal. Chem. 73 (1976) 125–128.
[48] M. Morita, C. Iwakura, H. Tamura, The anodic characteristics of modified Mn oxide electrode: Ti/RuOx/MnOx, Electrochim. Acta 23 (1978) 331–335, https://doi.org/10.1016/0013-4686(78)80070-X.
[49] J.L. Fernandez, M.R.G. DE Chialvo, A.C. Chialvo, Preparation and electrochemical characterization of Ti / $Ru_xMn_{1-x}O_2$ electrodes, J. Appl. Electrochem. 2 (2002) 513–520.
[50] M. Guglielmi, P. Colombo, V. Rigato, Compositional and microstructural characterization of RuO2-Ti02 catalysts synthesized by the sol-gel method, J. Electrochem. Soc. 139 (1992) 1655–1661.
[51] D.J. Morgan, Resolving ruthenium: XPS studies of common ruthenium materials, Surf. Interface Anal. 47 (2015) 1072–1079, https://doi.org/10.1002/sia.5852.
[52] A. Goryachev, L. Gao, Y. Zhang, R.Y. Rohling, R.H.J. Vervuurt, A.A. Bol, J.P. Hofmann, E.J.M. Hensen, Stability of CoP x electrocatalysts in continuous and interrupted acidic electrolysis of water, ChemElectroChem. 5 (2018) 1230–1239, https://doi.org/10.1002/celc.201701119.
[53] A. Goryachev, L. Gao, R.P.J. van Veldhoven, J.E.M. Haverkort, J.P. Hofmann, E.J.M. Hensen, On the origin of the photocurrent of electrochemically passivated p-InP(100) photoelectrodes, Phys. Chem. Chem. Phys. 20 (2018) 14242–14250, https://doi.org/10.1039/C8CP00894A.
[54] M. Aparicio, L. Klein, Thin and thick RuO_2-TiO_2 coatings on titanium substrates by the sol-gel process, J. Solgel Sci. Technol. 29 (2004) 81–88, https://doi.org/10.1023/B:JSST.0000023009.27548.02.
[55] M.C. Biesinger, B.P. Payne, A.P. Grosvenor, L.W.M. Lau, A.R. Gerson, R.S.C. Smart, Resolving surface chemical states in XPS analysis of first row transition metals, oxides and hydroxides: Cr, Mn, Fe, Co and Ni, Appl. Surf. Sci. 257 (2011) 2717–2730, https://doi.org/10.1016/j.apsusc.2010.10.051.
[56] V.R. Galakhov, M. Demeter, S. Bartkowski, M. Neumann, N.A. Ovechkina, E.Z. Kurmaev, N.I. Lobachevskaya, Y.M. Mukovskii, J. Mitchell, D.L. Ederer, Mn 3s exchange splitting in mixed-valence manganites, Phys. Rev. B - Condens. Matter Mater. Phys. 65 (2002) 1–4, https://doi.org/10.1103/PhysRevB.65.113102.
[57] M. Chigane, M. Ishikawa, Manganese oxide thin film preparation by Potentiostatic Electrolyses and electrochromism, J. Electrochem. Soc. 147 (2000) 2246, https://doi.org/10.1149/1.1393515.
[58] Y. Gorlin, T.F. Jaramillo, A bifunctional nonprecious metal catalyst for oxygen reduction and water oxidation, J. Am. Chem. Soc. 132 (2010) 13612–13614, https://doi.org/10.1021/ja104587v.
[59] A.J. Nelson, J.G. Reynolds, J.W. Roos, Core-level satellites and outer core-level multiplet splitting in Mn model compounds, J. Vac. Sci. Technol. A 18 (2000) 1072–1076, https://doi.org/10.1116/1.582302.
[60] T.L. Barr, Nature of the use of adventitious carbon as a binding energy standard, J. Vac. Sci. Technol. A 13 (1995) 1239, https://doi.org/10.1116/1.579868.
[61] P. Shrivastava, M.S. Moats, Wet film application techniques and their effects on the stability of RuO_2-TiO_2 coated titanium anodes, J. Appl. Electrochem. 39 (2009) 107–116, https://doi.org/10.1007/s10800-008-9643-y.
[62] V. Trieu, B. Schley, H. Natter, J. Kintrup, A. Bulan, R. Hempelmann, RuO_2-based anodes with tailored surface morphology for improved chlorine electro-activity, Electrochim. Acta 78 (2012) 188–194, https://doi.org/10.1016/j.electacta.2012.05.122.
[63] R. Frydendal, E.A. Paoli, B.P. Knudsen, B. Wickman, P. Malacrida, I.E.L. Stephens, I. Chorkendorff, Benchmarking the stability of oxygen evolution reaction catalysts: the importance of monitoring mass losses, ChemElectroChem. 1 (2014) 2075–2081, https://doi.org/10.1002/celc.201402262.
[64] M. Tahir, L. Pan, F. Idrees, X. Zhang, L. Wang, J.J. Zou, Z.L. Wang, Electrocatalytic oxygen evolution reaction for energy conversion and storage: a comprehensive review, Nano Energy 37 (2017) 136–157, https://doi.org/10.1016/j.nanoen.2017.05.022.
[65] R.L. Doyle, I.J. Godwin, M.P. Brandon, M.E.G. Lyons, Redox and electrochemical water splitting catalytic properties of hydrated metal oxide modified electrodes, Phys. Chem. Chem. Phys. 15 (2013) 13737, https://doi.org/10.1039/c3cp51213d.
[66] J. Kim, P.C. Shih, K.C. Tsao, Y.T. Pan, X. Yin, C.J. Sun, H. Yang, High-performance pyrochlore-type yttrium ruthenate electrocatalyst for oxygen evolution reaction in acidic media, J. Am. Chem. Soc. 139 (2017) 12076–12083, https://doi.org/10.1021/jacs.7b06808.
[67] Y.H. Fang, Z.P. Liu, Mechanism and tafel lines of electro-oxidation of water to oxygen on RuO_2(110), J. Am. Chem. Soc. 132 (2010) 18214–18222, https://doi.org/10.1021/ja1069272.
[68] H.S. Oh, H.N. Nong, T. Reier, A. Bergmann, M. Gliech, J. Ferreira De Araújo, E. Willinger, R. Schlögl, D. Teschner, P. Strasser, Electrochemical catalyst-support effects and their stabilizing role for IrO_x Nanoparticle catalysts during the oxygen evolution reaction, J. Am. Chem. Soc. 138 (2016) 12552–12563, https://doi.org/10.1021/jacs.6b07199.
[69] O. Diaz-Morales, S. Raaijman, R. Kortlever, P.J. Kooyman, T. Wezendonk, J. Gascon, W.T. Fu, M.T.M. Koper, Iridium-based double perovskites for efficient water oxidation in acid media, Nat. Commun. 7 (2016), https://doi.org/10.1038/ncomms12363.
[70] S. Sun, H. Li, Z.J. Xu, Impact of surface area in evaluation of catalyst activity, Joule. 2 (2018) 1024–1027, https://doi.org/10.1016/j.joule.2018.05.003.
[71] E. Tsuji, A. Imanishi, K.I. Fukui, Y. Nakato, Electrocatalytic activity of amorphous RuO_2 electrode for oxygen evolution in an aqueous solution, Electrochim. Acta 56 (2011) 2009–2016, https://doi.org/10.1016/j.electacta.2010.11.062.
[72] T. Oellers, L. Fruchter, E. Pizzutilo, S. Geiger, O. Kasian, M. Ledendecker, A.M. Mingers, S. Cherevko, M.T.M. Koper, K.J.J. Mayrhofer, Z. Li, O. Diaz-Morales, A. Ludwig, W.T. Fu, The stability number as a metric for electrocatalyst stability benchmarking, Nat. Catal. 1 (2018) 508–515, https://doi.org/10.1038/s41929-018-0085-6.
[73] M. Huynh, T. Ozel, C. Liu, E.C. Lau, D.G. Nocera, Design of template-stabilized active and earth-abundant oxygen evolution catalysts in acid, Chem. Sci. 8 (2017) 4779–4794, https://doi.org/10.1039/c7sc01239j.
[74] O.V. Boytsova, T.O. Shekunova, A.E. Baranchikov, Nanocrystalline manganese dioxide synthesis by microwave-hydrothermal treatment, Russ. J. Inorg. Chem. 60 (2015) 546–551, https://doi.org/10.1134/S0036023615050022.
[75] X. Shi, S. Siahrostami, G.-L. Li, Y. Zhang, P. Chakthranont, F. Studt, T.F. Jaramillo, X. Zheng, J.K. Nørskov, Understanding activity trends in electrochemical water oxidation to form hydrogen peroxide, Nat. Commun. 8 (2017) 701, https://doi.org/10.1038/s41467-017-00585-6.
[76] S. Cherevko, Electrochemical dissolution of noble metals native oxides, J. Electroanal. Chem. 787 (2017) 11–13, https://doi.org/10.1016/j.jelechem.2017.01.029.
[77] S. Cherevko, A.R. Zeradjanin, A.A. Topalov, N. Kulyk, I. Katsounaros, K.J.J. Mayrhofer, Dissolution of noble metals during oxygen evolution in acidic media, ChemCatChem. 6 (2014) 2219–2223, https://doi.org/10.1002/cctc.201402194.
[78] S. Cherevko, S. Geiger, O. Kasian, N. Kulyk, J.P. Grote, A. Savan, B.R. Shrestha, S. Merzlikin, B. Breitbach, A. Ludwig, K.J.J. Mayrhofer, Oxygen and hydrogen evolution reactions on Ru, RuO_2, Ir, and IrO_2 thin film electrodes in acidic and alkaline electrolytes: a comparative study on activity and stability, Catal. Today 262 (2016) 170–180, https://doi.org/10.1016/j.cattod.2015.08.014.
[79] E. Fabbri, A. Habereder, K. Waltar, R. Kotz, T.J. Schmidt, Developments and perspectives of oxide-based catalysts for the oxygen evolution reaction, Catal. Sci. Technol. 4 (2014) 3800–3821, https://doi.org/10.1039/C4CY00669K.
[80] R. Kötz, S. Stucki, D. Scherson, D.M. Kolb, In-situ identification of RuO_4 as the corrosion product during oxygen evolution on ruthenium in acid media, J. Electroanal. Chem. Interfacial Electrochem. 172 (1984) 211–219, https://doi.org/10.1016/0022-0728(84)80187-4.
[81] M. Wohlfahrt-Mehrens, J. Heitbaum, Oxygen evolution on Ru and RuO_2 electrodes studied using isotope labelling and on-line mass spectrometry, J. Electroanal. Chem. Interfacial Electrochem. 237 (1987) 251–260, https://doi.org/10.1016/0022-0728(87)85237-3.
[82] I.V. Artamonova, I.G. Gorichev, E.B. Godunov, Kinetics of manganese oxides dissolution in sulphuric acid solutions containing oxalic acid, Engineering 05 (2013) 714–719, https://doi.org/10.4236/eng.2013.59085.